Activated vibrational modes and Fermi resonance in tip-enhanced Raman spectroscopy

Mengtao Sun, Yurui Fang, Zhenyu Zhang, and Hongxing Xu

Phys. Rev. E **87**, 020401 — Published 13 February 2013

DOI: 10.1103/PhysRevE.87.020401

Activated Vibrational Modes and Fermi Resonance in Tip-Enhanced Raman Spectroscopy

Mengtao Sun, [1] Yurui Fang,[1] Zhenyu Zhang [2, 3] and Hongxing Xu [1, 4, 5*]

[1] *Beijing National Laboratory for Condensed Matter Physics, Institute of Physics, Chinese Academy of Sciences, P. O. Box 603-146, Beijing, 100190, People's Republic of China*

[2] *ICQD, Hefei National Laboratory at the Microscale, University of Science & Technology of China, Hefei, People's Republic of China*

[3] *Department of Physics and Astronomy, University of Tennessee, Knoxville, TN 37996-1200*

[4] *Division of Solid State Physics, Lund University, Lund 22100, Sweden*

[5] *The Center of Nanoscience and Technology, and School of Physics and Technology, Wuhan University, Wuhan 430072, People's Republic of China*

ABSTRACT

Using p-aminothiophenol (PATP) molecules on a gold substrate and high vacuum tip-enhanced Raman spectroscopy (HV-TERS), we show that the vibrational spectra of these molecules are distinctly different from those in typical surface-enhanced Raman spectroscopy. Detailed first-principles calculations help to assign the Raman peaks in the TERS measurements as Raman active and infrared (IR) active vibrational modes of dimercaptoazobenzene (DMAB), providing strong spectroscopic evidence for the dimerization of PATP molecules to DMAB under the TERS setup. The activation of the IR active modes is due to enhanced electromagnetic field gradient effects within the gap region of the highly asymmetric tip-surface geometry. Fermi resonances are also observed in HV-TERS. These findings help to broaden the versatility of TERS as a promising technique for ultrasensitive molecular spectroscopy.

PACS number: 33.20.Fb, 68.43.Pq, 73.20.Mf, 33.80.-b.

First demonstrated by Stöckle, Hayazawa, and Anderson in 2000 [1-3], tip-enhanced Raman spectroscopy (TERS) is a high-sensitivity optical analytical technique, with high spatial resolution beyond the diffraction limit of light. In TERS, a sharp metal tip is used to create a "hot site" to excite localized surface plasmons, and consequently enhance the electromagnetic field and Raman signals in the vicinity of the tip apex [1-9]. The tip can be moved in three dimensions to control the position of the "hot site" and the corresponding enhancement factor by changing the distance of the gap between the tip and the substrate. Therefore, TERS has the inherent advantage of overcoming one of the most severe restrictions in the application of surface enhanced Raman scattering (SERS), which usually requires roughness of metal surfaces or aggregations of metal nanoparticles to create "hot sites" that are difficult to control. TERS may solve a wide variety of problems in high vacuum (HV) single-crystal surface science, electrochemistry, heterogeneous catalysis, microelectronics, and tribology, offering new opportunities for gaining insights into the physics and chemistry of these diverse systems.

As a compelling and challenging example, the appearance of normally unseen Raman modes in the spectrum of p-aminothiophenol (PATP) adsorbed on metal surfaces has been a long-standing issue in SERS. Earlier explanations often attribute this phenomenon to selective enhancement of some b_2 modes of PATP due to charge transfer between the molecules and the metal substrates [10-13]. Recently, dimerization of PATP to dimercaptoazobenzene (DMAB) has been suggested to explain these unseen Raman modes [14-18]. Both theoretical simulations [14-15] and experimental observations [15-16] offer credible support to the explanation based on the dimerization mechanism; nevertheless, controversies remain regarding the dimerization explanation, due to the broadening and relatively few Raman modes in the SERS spectra [19-21]. It has been suggested that the gradient effect associated with the strongly enhanced electric field at a rough metal surface [22-24] could activate IR-active modes, which are usually Raman inactive. If the IR-active modes of DMAB are observed together with the Raman-active modes in SERS studies, it is expected that the dimerization picture will show more convincing spectroscopic evidence.

In this Letter, we exploit the advantage of TERS to investigate the long-standing issue of the appearance of new Raman modes of adsorbed PATP molecules, which are typically unseen in normal Raman spectroscopy. We observe many more and narrower Raman peaks in our high vacuum TERS (HV-TERS) system than in previous SERS studies. By comparing these experimental observations with our theoretical simulations within density functional theory, we can assign almost all the Raman peaks as Raman-active symmetric modes and IR-active asymmetric modes of the DMAB molecule. The fully activated and strongly enhanced IR-active modes as observed in our HV-TERS data give more convincing spectroscopic evidence to support the conversion of PATP via dimerization into the putative product DMAB. The gradient effect associated with the greatly enhanced electric field within the nanogap region between the sharp gold tip and gold film can activate the IR-active modes of the DMAB molecule to be Raman-active. The huge electromagnetic enhancement in the nanogap region further results in distinct Fermi resonances, characterized by strong coupling of a fundamental mode and an overtone of a different mode or a combinational mode, to split the corresponding Raman modes.

The schematic diagram of the HV-TERS system is shown in Fig. 1. It consists of a homemade scanning tunneling microscope (STM) in a high-vacuum chamber, a Raman spectrometer combined with side illumination of 632.8 nm He-Ne laser light with an angle of 60^{o} for Raman measurements, and three-dimensional piezo stages for the tip and sample manipulations. The pressure in the chamber is ~10^{-7} Pa. A gold tip with a ~50 nm radius was fabricated by electrochemical etching of a 0.25 mm diameter gold wire [25]. The substrate was prepared by evaporating a 100 nm gold film to a newly cleared mica film under high vacuum. The film was immersed in a 1×10^{-5} M PATP ethanol solution for 24 hours, then washed with ethanol for 10 minutes to guarantee that there was only one monolayer of PATP molecules adsorbed on the gold film. Then immediately the sample was put into the high-vacuum chamber. To get a good signal-to-noise ratio, the TERS signals were collected with an acquisition time of 60 seconds and accumulated 20 times for each spectrum.

We measured TERS of PATP adsorbed on the Au film at different bias voltages and currents, and found the optimal conditions to be ± 1 V (bias voltage on the sample) and 1 nA (current) in our HV-

TERS system. Two series of typical measured spectra using the experimental conditions described above for different biases are shown in Figs. 2(a) and 2(b), respectively. The fluctuations of these spectra are small, and the spectra are stable and can be readily repeated experimentally under these conditions. The profiles of the spectra obtained at +1 V and -1 V are quite similar, indicating that there is not much influence from the polarity of the bias voltage on the TERS measurement here. For comparison, the typical SERS spectrum of PATP in Au sol and the normal Raman scattering (NRS) spectrum of PATP powder (Fig. 2(c)) were also measured with a Renishaw inVia Raman system and excited with light at 632.8 nm. The molecular structure of DMAB and PATP are also shown in the insets of Fig. 2(c).

Comparing Figs. 2(a) and 2(b) with Fig. 2(c), it is found that the TERS peaks of PATP adsorbed on the Au film are significantly different from the SERS and NRS peaks of PATP. Many more and narrower Raman peaks are observed in Figs. 2(a) and 2(b) for the HV-TERS study than in Fig. 2(c) for the SERS and NRS studies. It is worthwhile to note that our previous report showed that the SERS peaks of PATP adsorbed on a bare Au film is very similar to the NRS of PATP [18], whereas the SERS peaks of PATP on Au colloidal nanoparticles is different from the corresponding NRS measurements. The latter case has been attributed to plasmon-assisted chemical reaction of PATP dimerization into DMAB, but not the case for the bare Au film where the plasmon enhancement is weak. The rich spectroscopic features in TERS could also suggest PATP dimerization due to a strong local electromagnetic enhancement within the nanogap region of the tip-surface geometry. Moreover, the polarity of the bias voltage does not influence the TERS profiles in Fig. 2(a) and Fig. 2(b), which may indicate that the detected molecule should be structurally symmetric, offering additional evidence for the formation of DMAB converted from PATP to bridge two metal surfaces symmetrically (the Au tip and the Au film) with two thiol groups. Nevertheless, the difference between TERS and SERS spectra remains.

To interpret the above spectral phenomena correctly, we choose two spectra at different biases for vibrational mode assignments as shown in Figs. 3(a) and 3(b). Furthermore, the Raman spectra of

DMAB were calculated within density functional theory [26] using the Gaussian 09 suite [27] with PW91PW91 functional [28], a 6-31G(d) basis set for C, N, S and H, and a LANL2DZ basis set [29] for Au, where a Au_5-DMAB-Au_5 junction was used to simulate the Raman spectra, mimicking the TERS setup. The IR spectra of DMAB in the Au_5-DMAB-Au_5 junction were also simulated with the same method. Based on the simulated Raman spectrum in Fig. 3(c), all the Raman-active symmetric ag vibrational modes in Figs. 3(a) and 3(b) can be assigned. Interestingly, most of the remaining Raman peaks in Figs. 3(a) and 3(b) can be assigned as IR-active asymmetric bu modes according to the simulated IR spectrum in Fig. 3(d). It has been previously studied that the gradient-field effect can activate IR-active modes in SERS due to molecular quadrupole transitions when the molecules are placed near metal surfaces [22, 23]. Such gradient-field effects were also observed in near-field optical microscopy Raman (NSOM-Raman) [24]. Similarly, the observation of the full activation of IR-active modes can be caused by very high field gradients within the nanogap of a highly asymmetric geometry, consisting of a sharp metal tip and a flat metal surface in our HV-TERS system. Moreover, the enormous electromagnetic field enhancement in the nanogap region makes this phenomenon of activation of IR-active modes more readily observable.

Next we compare the simulated Raman spectrum in Fig. 3(c) and the SERS peakes in Fig. 2(c). It is found that six strong peaks in the experimental and simulated results agree well with each other without scaling. We also note that in the simulated Raman spectrum of DMAB in Fig. 3(c), the wavenumbers have been scaled by an insignificant factor of 1.014 (or blue shifted by ~1%) for closer comparison with the TERS data shown in Figs. 3(a) and 3(b). Such blue shifts could easily be caused by weak external perturbations, such as tip, current, and voltage in the HV-TERS system.

Figure 4(a) shows a zoom-in spectrum of Fig. 3(a), where each of the symmetric and asymmetric C-N stretching modes, assigned as the Raman-active ag_{13} mode and IR-active asymmetric bu_{13} mode, respectively, splits into two Raman peaks. The splitting of the Raman peaks results from Fermi resonance (FR). In FR, an overtone of a different fundamental mode or a combination mode can appear in the vibrational spectra by gaining spectral weight from a fundamental mode [30]. FRs are frequently

found in IR or Raman spectra in symmetric triatomic molecules such as CO_2 and CS_2 [30-32], but this is the first time FR has been observed in a TERS study. When the molecules are placed in the nanogap region, external perturbations from greatly enhanced electromagnetic fields, high field gradients, and the Au tip could cause such distinct FRs.

For a FR, the split vibrational energies under the perturbation can be written as [30-32],

$$E_{\pm} = \frac{1}{2}(E_A + E_B) \pm \frac{1}{2}\sqrt{(E_A - E_B)^2 + 4\phi^2}\ , \tag{1}$$

where E_A and E_B are the vibrational energies of the fundamental mode and an overtone of a different fundamental mode (or a combination mode) before splitting, ϕ is the FR coupling coefficient, which describes the coupling strength of the fundamental vibrational mode and the combinational mode (or the overtone mode) in the FR. When the FR coupling coefficient is larger, the spectral energy splitting between the fundamental vibrational mode and the combinational mode (or the overtone mode) is also larger. In addition, when the unperturbed energies E_A and E_B in Eq. (1) are closer, the FR coupling coefficient becomes larger. For our case in Fig. 4(a), the unperturbed energies E_A and E_B for the Raman-active symmetric ag_{13} or the IR-active asymmetric bu_{13} can be estimated as:

$$E_A = \frac{E_+ + E_-}{2} + \frac{E_+ - E_-}{2} \times \frac{I_+ - I_-}{I_+ + I_-} \tag{2}$$

$$E_B = \frac{E_+ + E_-}{2} - \frac{E_+ - E_-}{2} \times \frac{I_+ - I_-}{I_+ + I_-}, \tag{3}$$

where I_+ and I_- are the Raman intensities of the split peaks. The difference in energy between the perturbed levels in the presence and absence of FR can be obtained with $\Delta E_{\pm} = E_+ - E_-$ and $\Delta E_{AB} = |E_A - E_B|$, respectively.

In Fig. 4(a), we obtain $I_+(ag_{13}) \approx I_-(g_{13})$ and $I_+(bu_{13}) \approx \frac{1}{2} I_-(bu_{13})$, $\Delta E_{\pm}(ag_{13}) = 20.4$ cm^{-1} and $\Delta E_{\pm}(bu_{13}) = 14.6$ cm^{-1}. For the Raman-active symmetric ag_{13} mode, according to Eqs. 2 and 3, we obtain $E_A = E_B = \frac{E_+ + E_-}{2}$, i.e. $\Delta E_{AB} \approx 0$ cm^{-1}, and the FR coupling coefficient can be calculated by

using Eq. 1 as $\phi(ag_{13}) = \frac{1}{2}\Delta E_{\pm}(ag_{13}) = 10.2$ cm^{-1}. As illustrated in Figs. 4(b) and 4(c) with different vibrational modes marked as short vertical lines, the fundamental Raman-active symmetric ag_{13} mode frequency at 1213 cm^{-1} is very close to the combinational mode frequency of ag_6 at 727 cm^{-1} and bg_6 at 485 cm^{-1} with $\Delta E_{AB} = E(ag_{13}) - [E(bg_6) + E(ag_6)] \approx 1$ cm^{-1}. The combinational mode $bg \times ag = bg$ is asymmetric.

For the IR-active asymmetric bu_{13} mode, we obtain $E_A = \frac{E_+ + E_-}{2} + \frac{1}{3} \times \frac{\Delta E_{\pm}}{2}$ and $E_B = \frac{E_+ + E_-}{2} - \frac{1}{3} \times \frac{\Delta E_{\pm}}{2}$, according to Eqs. 2 and 3, and $I_+(bu_{13}) \approx \frac{1}{2} I_-(bu_{13})$ as in Fig. 4(a). We can then obtain $\Delta E_{AB}(bu_{13}) = \frac{1}{3}\Delta E_{\pm}(bu_{13}) = 4.9$ cm^{-1} and $\phi(bu_{13}) = \frac{\sqrt{2}}{3}\Delta E_{\pm}(bu_{13}) = 6.88$ cm^{-1}. As illustrated in Figs. 4(b) and 4(c), the calculated IR-active asymmetric bu_{13} mode frequency at 1267 cm^{-1} is about 7 cm^{-1} smaller than the combinational mode of bu_5 at 634 cm^{-1} and bu_6 at 640 cm^{-1}. The difference between the experimental and theoretical values (4.9 cm^{-1} and 7 cm^{-1}) is about 2 cm^{-1}. The symmetry of the combinational mode is $bu \times bu = ag$ is symmetric.

In summary, by using the HV-TERS system, we have provided evidence for the conversion of PATP to DMAB via dimerization, possibly catalyzed by the presence of the TERS tip on top of the gold film. The observation in HV-TERS of the IR-active bands associated with DMAB molecules provides further experimental evidence for the dimerization mechanism. The activation of these extra modes is primarily attributed to enhanced electromagnetic field gradient effects within the gap region of the tip-surface geometry. Moreover, strongly enhanced plasmon responses in the nanogap region further results in distinct Fermi resonance to split the corresponding Raman peaks. These original findings are not only of fundamental significance, but also help to significantly broaden the capacity of TERS as an analytical tool for ultrasensive molecular spectroscopy.

ACKNOWLEDGMENT: This work was supported by the National Basic Research Project of China (Grants 2012YQ12006005, 2009CB930701, 2009CB930704 and 2007CB936804), the National Natural Science Foundation of China (Nos. 90923003, 10874233, 10874234, 20703064 and 11034006, 11227407), "Knowledge Innovation Project" (KJCX2-EW-W04) of CAS, the U.S. National Science Foundation (Grant No. 0906025), the U.S. Department of Energy, Basic Energy Sciences, Materials Sciences and Engineering Division, and the Nanometer Structure Consortium at Lund University, nmC@LU (H.X.X).

References and notes:

* Corresponding author: hxxu@iphy.ac.cn (H. X. Xu).

1. R. M. Stöckle, Y. D. Suh, V. Deckert and R. Zenobi, Chem. Phys. Lett. **318**, 131 (2000).
2. N. Hayazawa, Y. Inouye, Z. Sekkat and S. Kawata, Opt. Commun.**183**, 333 (2000).
3. M. S. Anderson, Appl. Phys. Lett. **76**, 3130 (2000).
4. B. Pettinger, B. Ren, G. Picardi, R. Schuster and G. Ertl, Phys. Rev. Lett. **92**, 096101 (2004).
5. W. Zhang, X. Cui, B. S. Yeo, T. Schmid, C. Hafner and R. Zenobi, Nano Lett. **7**, 1401 (2007).
6. E. Bailo and V. Deckert, Chem. Soc. Rev. **37**, 921 (2008).
7. J. Steidtner and B. Pettinger, Phys. Rev. Lett. **100**, 236101 (2008).
8. M. T. Sun, Z. L. Zhang, H. R. Zheng and H. X. Xu, Sci. Rep. **2**, 647 (2012).
9. N. Jiang, E. T. Foley, J. M. Klingsporn, M. D. Sonntag, N. A. Valley, J. A. Dieringer, T.; Seideman, G. C. Schatz, M. C. Hersam, R. P. Van Duyne, Nano Lett. **12**, 5061 (2012).
10. M. Osawa, N. Matruda, K. Yoshii and I. Uchida, J. Phys. Chem. **98**, 12702 (1994).
11. A. Campion and P. Kambhampati, Chem. Soc. Rev. **27**, 241(1998).
12. Q. Zhou, X. Li, Q. Fan, X. Zhang and J. Zheng, Angew. Chem. Int. Ed. **45**, 3970 (2006).
13. T. Shegai, A. Vaskevich, I. Rubinstein and G. Haran, J. Am. Chem. Soc. **131**, 14390 (2009).
14. D. Y. Wu, X. M. Liu, Y. F. Huang, B. Ren, X. Xu and Z. Q. Tian, J. Phys.Chem. C 113, 18212 (2009).
15. Y. R. Fang, Y. Z. Li, H. X. Xu and M. T. Sun, Langmuir **26**, 7737 (2010).
16. Y. F. Huang, H. P. Zhu, G. K. Liu, D. Y. Wu, B. Ren and. Z. Q. Tian, J. Am. Chem. Soc. **132**, 9244 (2010).
17. M. T. Sun and H. X. Xu, Small **8**, 2777 (2012).
18. Y. Z. Huang, Y. R. Fang, Z. L. Yang and M. T. Sun, J. Phys. Chem. C **114**, 18263 (2010).
19. W.-H. Park and Z. H. Kim, Nano Lett. **10**, 4040 (2010).
20. K. Kim, D. Shin, H. B. Lee and K. S. Shin, Chem. Commun. **47**, 2020 (2011).
21. W. Ji, N. Spegazzini, Y. Kitahama, Y. Chen, B. Zhao and Y. Ozaki, J. Phys. Chem. Lett. **3**, 3204

(2012).

22. M. Moskovits and D. P. DiLella, J. Chem. Phys. **73**, 6068 (1980).
23. M. Moskovits and D. P. DiLella, J. Chem. Phys. **77**, 1655 (1982).
24. E. J. Ayars, H. D. Hallen and C. L. Jahncke, Phys. Rev. Lett. **85**, 4180 (2000).
25. B. Ren, G. Picardi and B. Pettinger, Rev. Sci. Instrum. **75**, 837 (2004).
26. P. Hohenberg and W. Kohn, Phys. Rev. **136**, B864 (1964).
27. M. J. Frisch, et al., **Gaussian 09**, Revision A.02, Gaussian, Inc., Wallingford CT, 2009.
28. J. P. Perdew, K. Burke and Y. Wang, Phys. Rev. B **54**, 16533 (1996).
29. P. J. Hay and W. R. Wadt, J. Chem. Phys. **82**, 270 (1985).
30. E. Fermi, Z. Phys. **71**, 250 (1931).
31. R. A. Nyquist, H.A. Fouchea, G.A. Hoffman and D. L. Hasha, Appl. Spectrsoc. **45**, 860 (1991).
32. K. D. Bier and H. J. Jodi, J. Chem. Phys. **86**. 4406 (1987).

Figure captions

Figure 1. (color on line) Schematic diagram of the home-built HV-TERS setup.

Figure 2. (a) and (b) Spectra of DMAB under experimental conditions of 1 nA current, +1 V, and -1 V bias voltage, respectively, measured at different positions with the HV-TERS system. (c) SERS peaks of DMAB in Au sol and the normal Raman scattering spectrum of PATP.

Figure 3. (color on line) (a) and (b) TERS peaks of DMAB under experimental conditions of 1 nA current, -1 V and +1 V bias voltage, respectively. (c) Simulated Raman and (d) IR spectra of DMAB, where the wavenumber is scaled by 1.014.

Figure 4. (color on line) (a) Experimentally observed FR and simulated TERS peaks of DMAB for the Raman-active symmetric ag_{13} and IR-active asymmetric bu_{13} modes. (b) and (c) Calculated vibrational modes and the combinational modes for FR, where the wavenumber is scaled by 1.014.

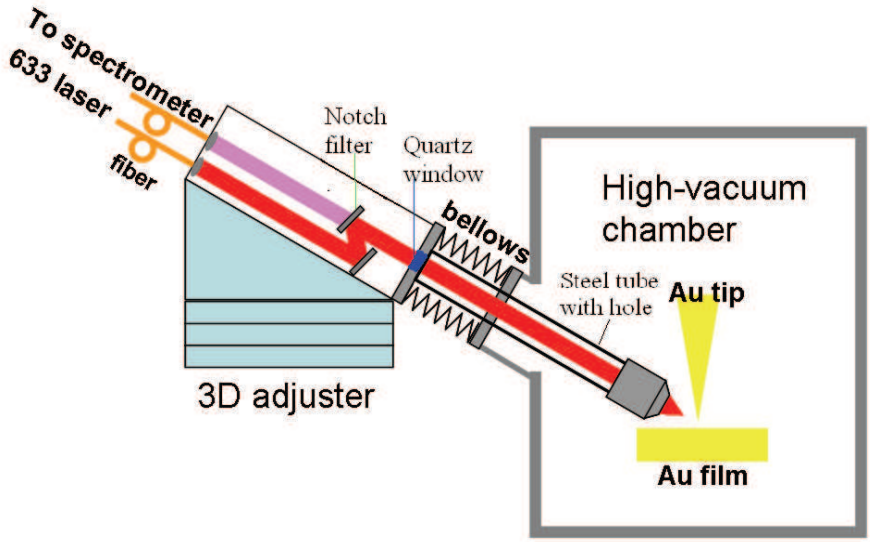

Figure 1 LH13404ER 04FEB2013

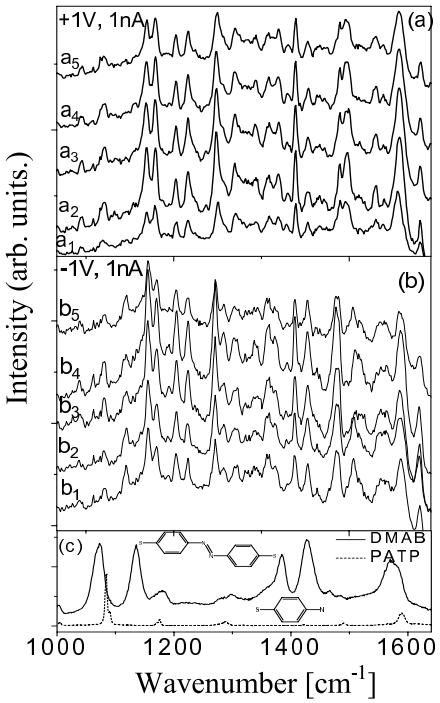

Figure 2 LH13404ER 04FEB2013

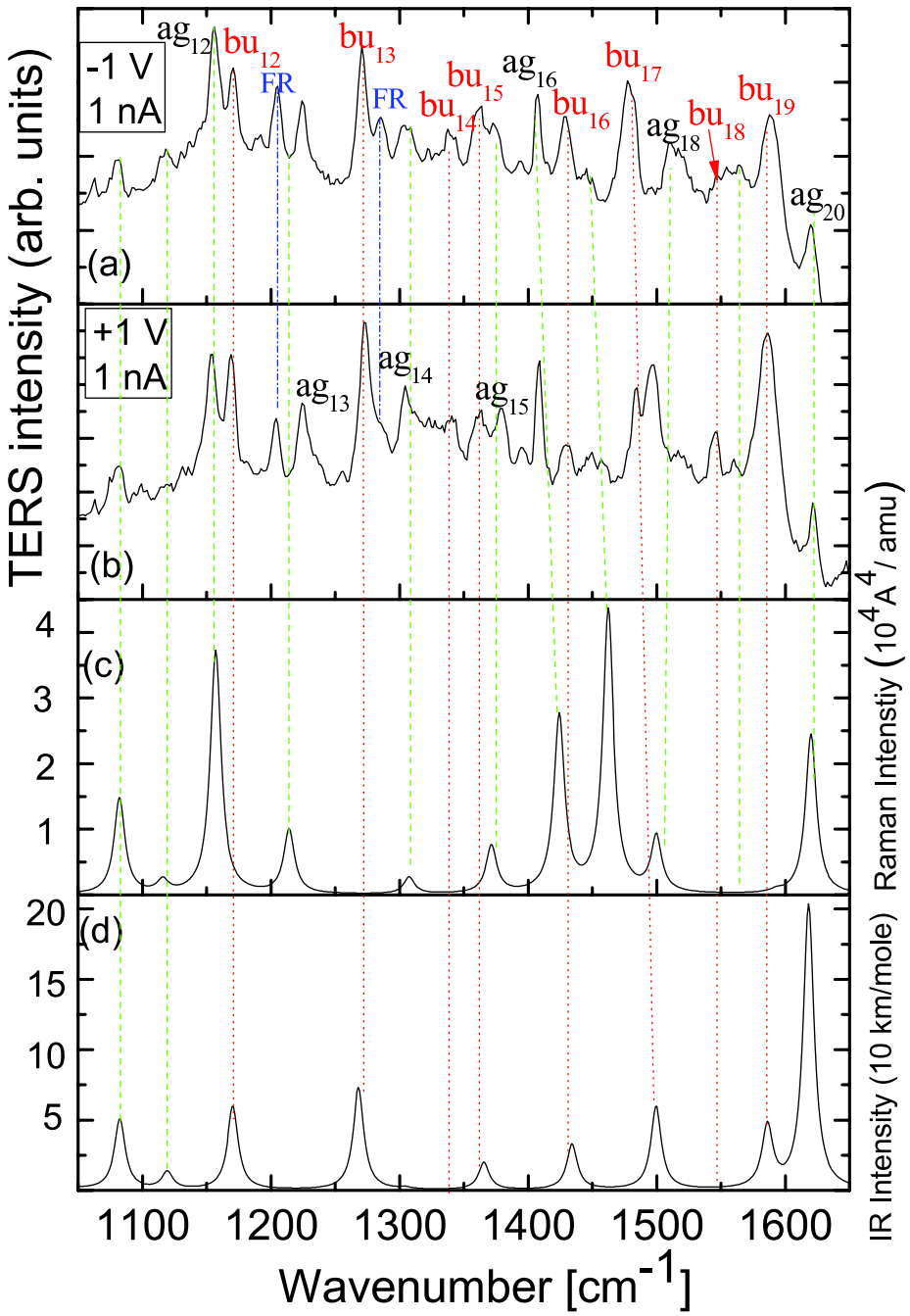

1

Figure 3 LH13404ER 04FEB2013

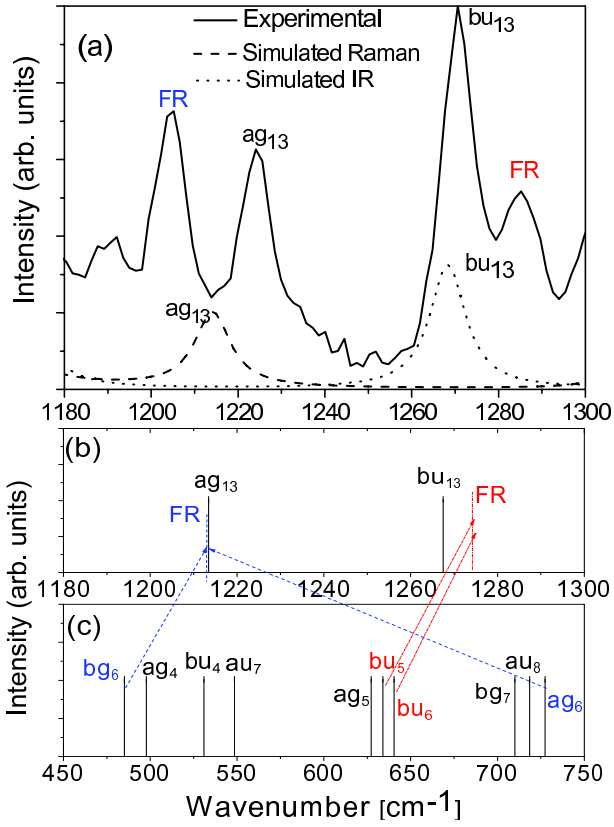

Figure 4 LH13404ER 04FEB2013